applied sciences

MDPI

Article

Research on Radionuclide Identification Method Based on GASF and Deep Residual Network

Shuqiang Zhao [1,2], Shumin Zhou [1,*] and Rui Chen [1]

[1] Jiangxi Engineering Research Center of Process and Equipment for New Energy, East China University of Technology, Nanchang 330013, China; sqzhao999@163.com (S.Z.); chenrui@ecut.edu.cn (R.C.)
[2] School of Information Engineering, East China University of Technology, Nanchang 330013, China
* Correspondence: smzhou@ecut.edu.cn

Featured Application: This article proposes the application of the GASF method to process energy spectrum data, preserving the interdependencies of feature information within the spectrum. By effectively extracting spatial features from the data, the method enhances the accuracy of nuclide identification.

Abstract: In nuclide identification, traditional methods based on nuclide library comparisons rely on the identification of characteristic peaks, often overlooking the full spectrum information, which leads to cumbersome operations and low efficiency. In recent years, machine learning and deep learning techniques have been introduced into the field of nuclide recognition to improve identification efficiency; however, most existing methods fail to effectively extract deep features from the data. To address this issue, this paper proposes a method that integrates the Gram Angular Summation Field (GASF) algorithm with a Deep Residual Network (ResNet) for processing nuclide energy spectrum data. First, the GASF algorithm is used to transform one-dimensional spectral data into two-dimensional images, thereby fully extracting spatial features from the data. Then, these two-dimensional images are input into the ResNet model, where features are automatically extracted through multiple convolutional layers. Finally, the Softmax layer is used for nuclide classification. Experimental results demonstrate that the proposed method can effectively improve both the accuracy and efficiency of nuclide identification; the recognition accuracy on the simulated data reaches 99.5%, and, when tested with actual measurement data containing unknown radionuclides, the model still achieves a high accuracy of 92.6%. This study shows that the combination of deep learning and signal processing techniques can significantly improve the accuracy and application scope of nuclide identification, offering substantial practical value.

Keywords: ResNet; GASF; neural network; nuclide identification

check for updates

Academic Editor: Roberta Sparvoli

Received: 5 November 2024
Revised: 16 January 2025
Accepted: 21 January 2025
Published: 24 January 2025

Citation: Zhao, S.; Zhou, S.; Chen, R. Research on Radionuclide Identification Method Based on GASF and Deep Residual Network. *Appl. Sci.* **2025**, *15*, 1218. https://doi.org/10.3390/app15031218

Correction Statement: This article has been republished with a minor change. The change does not affect the scientific content of the article and further details are available within the backmatter of the website version of this article.

Copyright: © 2025 by the authors. Licensee MDPI, Basel, Switzerland. This article is an open access article distributed under the terms and conditions of the Creative Commons Attribution (CC BY) license (https://creativecommons.org/licenses/by/4.0/).

1. Introduction

Nuclide identification is the process of determining the type of a nuclide by analyzing the radiation signals emitted by radioactive materials, such as gamma rays. Nuclide identification technology has a wide range of applications across various fields. In nuclear safety and non-proliferation, it is used for nuclear security checks, border control, monitoring nuclear materials during transportation, and preventing illegal entry into unsafe areas. In environmental monitoring, it helps track radiation contamination following nuclear accidents and aids in the management of nuclear waste. In the medical field, it is applied in diagnostic imaging, radioactive drug monitoring, and precise localization in radiation

therapy. In the nuclear energy sector, it enables real-time monitoring of nuclear reactor operations and nuclear fuel inspections. In scientific research, it is employed in astrophysics for studying elemental composition, in archaeology for isotopic dating, and in ecology for assessing radioactive contamination. In industrial applications, it is used in nuclear radiography, radioactive source detection, and ensuring the safe use of smoke detectors, among other applications [1–4]. The accurate identification of radioactive materials is critical for preventing the illegal use of nuclear substances and ensuring public safety. The traditional nuclide library comparison method relies primarily on characteristics such as the position and area of spectral peaks, comparing these with a standard nuclide library to identify the nuclide type [5–7]. However, this method primarily focuses on spectral peaks, overlooks the full spectrum's potential, and is inefficient and cumbersome to apply. As such, traditional methods face significant challenges in accurately identifying nuclides.

In recent years, with the rise of artificial intelligence, many researchers have applied machine learning and deep learning techniques to nuclide recognition, aiming to enhance recognition efficiency. Machine learning methods include logistic regression [8], fuzzy decision trees [9], singular value decomposition (SVD), support vector machines (SVMs) [10], and Bayesian networks [11], among others. Deep learning techniques include Long Short-Term Memory (LSTM) networks [12] and Convolutional Neural Networks (CNNs) [13]. Wenqing Zhou employed logistic regression and wavelet packet decomposition to extract feature vectors from gamma spectrum data for training, achieving an identification accuracy of 97% [8]. Jun Song Ren developed a nuclide recognition algorithm based on singular value decomposition (SVD) and support vector machines (SVMs), converting one-dimensional gamma spectra into two-dimensional images, extracting feature vectors, and building a classifier. The recognition rate for nuclides reached 98% [10]. Yao Wang used Long Short-Term Memory (LSTM) networks for nuclide gamma spectrum identification and compared them with BP neural networks and Convolutional Neural Networks (CNNs). The average recognition rates on the test set were 83.45% and 86.21%, respectively, while the LSTM model achieved an average recognition rate of 93.04% [12]. However, traditional machine learning methods often rely on manual feature extraction and selection, which limits their ability to capture deep features and complex patterns in the data. In deep learning, most researchers typically input one-dimensional spectral data directly into models or convert it into grayscale images [14]. One-dimensional sequence data are often not subjected to feature extraction, making it difficult to capture complex patterns effectively. Furthermore, such data lack spatial structure and cannot fully utilize local features. Although grayscale images convey information through pixel values, their static nature hinders the extraction of time-dependent features, preventing the detection of subtle changes or higher-order patterns in the data.

To address the aforementioned challenges, this paper employs deep neural networks to adaptively process input signals and automatically extract features, showcasing their significant advantages in image recognition. From the perspective of the entire energy spectrum, the dependency between counts and channel addresses is taken into account. A novel radioactive nuclide identification method is proposed, which uses the Gram Angular Summation Field (GASF) algorithm for data processing and integrates it with the ResNet deep residual network. First, to address the issue of im137lanced counts in the energy spectrum, the PAA algorithm is applied for dimensionality reduction. Then, the GASF algorithm is used to transform the one-dimensional data into two-dimensional images, fully leveraging the spatial features and dependencies within the data. Next, the two-dimensional images are fed into a deep residual network, where multiple rounds of convolution automatically extract features. Finally, the Softmax layer is employed for

nuclide classification, and the effectiveness and accuracy of the proposed method are validated through comparative experiments.

2. Energy Spectrum Two-Dimensional Method Based on Segmented GSAF

The Gramian Angular Field (GAF) is an encoding technique used to transform sequence data into two-dimensional images [15]. Its fundamental concept is to capture the interdependencies and dynamic characteristics of sequence data through polar coordinate transformation. The process involves converting one-dimensional sequence data into polar coordinates and then using trigonometric functions to construct a two-dimensional GAF matrix. Each element in the matrix corresponds to a pixel in the resulting image. By applying a suitable color mapping, the structure and patterns of the matrix can be visually represented. The GAF can be classified into two types based on the encoding method: Gram Angular Summation Field (GASF) and Gram Angular Difference Field (GADF), depending on whether cosine sums or sine differences are used. GADF focuses on capturing the differences between data points. In nuclide identification, the primary objective is to identify stable patterns and similarities in spectral data, as well as to determine the consistent characteristics of the same nuclide under different conditions. GASF emphasizes the similarity between data points, which helps reveal the inherent features in nuclide spectra and improves the recognition of signal structures. Therefore, this paper utilizes GASF for data processing. The conversion process is outlined as follows: normalize the raw energy spectrum data set $Y = [y_1, y_2, y_3, \ldots, y_N]$ as per Equation (1).

$$\overline{Y}_i = \frac{(y_i - \max(Y)) + (y_i - \min(Y))}{\max(Y) - \min(Y)} \tag{1}$$

In the formula, $\overline{Y}_i$ represents the normalized value of the ith channel in the original energy spectrum; y_i is the count of the i-th track in the original spectrum; $Max(Y)$ is the maximum count and $Min(Y)$ is the minimum count in the original energy spectrum. The normalized data are $\overline{Y} = [\overline{y}_1, \overline{y}_2, \overline{y}_2, \ldots \overline{y}_N]$, with a range of [−1,1]. The normalized data are then transformed according to Equation (2) to obtain the angle φ_i and corresponding radius r_i in polar coordinates.

$$\begin{cases} \varphi_i = \arccos(\overline{Y}_i), & -1 \le \overline{Y}_i \le 1 \\ r_i = \frac{N_i}{N}, & N_i = 1, 2, 3 \ldots, 1024 \end{cases} \tag{2}$$

After converting to polar coordinates, the angle φ has a range of [0, π]. The corresponding polar radius r_i is represented by the ratio of the channel number N_i of the energy spectrum data point y_i to the total number of channels N, where N = 1024 in this study. Then, the Gram matrix, defined by the sum of cosine functions between each pair of data points, is used to construct the Gram Angular Field (GAF), as shown in Equation (3).

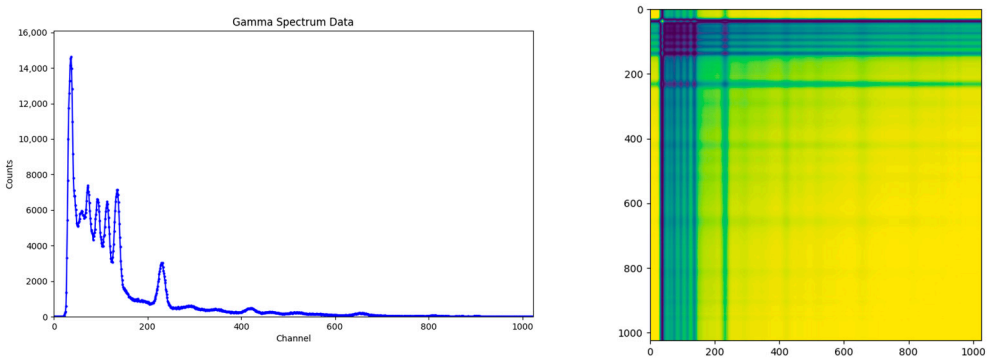
$$\begin{aligned} Gram &= \begin{bmatrix} \cos(\varphi_1 + \varphi_1) & \ldots & \cos(\varphi_1 + \varphi_N) \\ \cos(\varphi_2 + \varphi_1) & \ldots & \cos(\varphi_2 + \varphi_N) \\ \cdots & \cdots & \cdots \\ \cos(\varphi_N + \varphi_1) & \ldots & \cos(\varphi_N + \varphi_N) \end{bmatrix} \\ &= \overline{Y}' \cdot \overline{Y} - \sqrt{I - \overline{Y}^2}' \cdot \sqrt{I - \overline{Y}^2} \end{aligned} \tag{3}$$

Here, $I = [1,\ 1,\ 1,\ \ldots,\ 1]$ is a unit row vector. Then, the inner product of two numbers is defined according to Equation (4), and Equation (3) is transformed to obtain the Gram Angular Summation Field (GASF), as shown in Equation (5).

$$\begin{aligned} \langle a, b \rangle &= cos(a+b) = cos\{\arccos(a) + \arccos(b)\} \\ &= cos\{\arccos(a)\} \cdot cos\{\arccos(b)\} - sin\{\arccos(a)\} \cdot sin\{\arccos(a)\} \\ &= a \cdot b - \sqrt{1-a^2} \cdot \sqrt{1-b^2} \end{aligned} \tag{4}$$

$$GASF = \begin{bmatrix} \langle \overline{y}_1, \overline{y}_1 \rangle & \cdots & \langle \overline{y}_1, \overline{y}_N \rangle \\ \langle \overline{y}_2, \overline{y}_1 \rangle & \cdots & \langle \overline{y}_2, \overline{y}_N \rangle \\ \cdots & \cdots & \cdots \\ \langle \overline{y}_N, \overline{y}_1 \rangle & \cdots & \langle \overline{y}_N, \overline{y}_N \rangle \end{bmatrix} \tag{5}$$

Each element *GASF*(*i*,*j*) in the matrix represents the cosine similarity between the data points at the *i*-th row and *j*-th column. This method of construction effectively captures the interrelationships between the data points and reflects the inherent structure of the energy spectrum data sequence. It enables the two-dimensional transformation of energy spectrum data through the *GASF* conversion. An example of the conversion result is shown in Figure 1.



(**a**) (**b**)

Figure 1. Two-dimensional transformation of energy spectrum based on GASF: (**a**) original energy spectrum data; (**b**) data after GASF conversion.

The energy spectrum data in this study consist of 1024 track addresses. After applying GASF, the resulting image has a size of 1024 × 1024. Due to the high dimensionality, it is not suitable for subsequent processing. As shown in Figure 1a, the counts in the first 300 channels are significantly higher than those in the remaining channels. If GASF is applied directly, the information from low-count channels will be overwhelmed. To facilitate further experiments and minimize the loss of original information, the Piecewise Aggregate Approximation (PAA) algorithm is applied to reduce the dimensionality of the original energy spectrum data before GASF conversion [16]. Specifically, the 1024 energy spectrum data are divided into 16 subsequences, each containing 64 channels. These subsequences are compressed using the PAA algorithm (k = 2), and GASF conversion is then applied to each compressed subsequence. After dimensionality reduction using the PAA algorithm, the original 1024 energy spectrum data are transformed into a 16 × 32 × 32 matrix through GASF conversion. An appropriate color mapping is chosen to convert this matrix into two-dimensional image data. Segmented GASF is used to process the energy spectrum data, with conversion results for channels 1–192 and 513–704, as shown in Figure 2a and Figure 2b, respectively. From the figure, it can be seen that the transformed images of different channel addresses preserve their respective feature information.

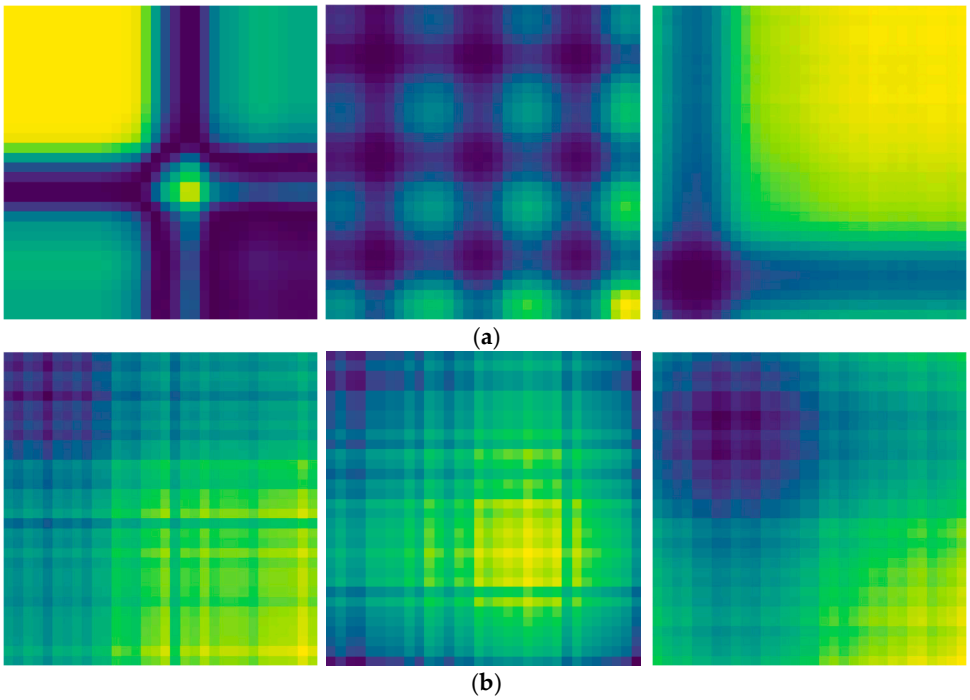


Figure 2. Two-dimensional representation of the energy spectrum based on segmented GASF: (**a**) segmented GASF conversion for channels 1–192; (**b**) segmented GASF conversion for channels 513–704.

3. Establishment of Neural Network Model

3.1. Modeling

Early convolutional neural networks primarily relied on simple stacking of convolutional layers, pooling layers, and fully connected layers to increase the network depth. Data were transmitted layer by layer from the input to the output through hierarchical connections. However, as the depth of the network increased, the weights failed to update or updated insignificantly, leading to the vanishing or exploding gradient problem, which hindered effective network training. To address this issue, Kaiming He et al. proposed the deep convolutional neural network ResNet (Residual Network) [17], which mitigates the training degradation problem in deep networks by introducing residual connections. In a traditional convolutional neural network, as shown in Figure 3A, the output H(X) = F(X) is obtained after the input X passes through the convolutional layer and activation function. In contrast, the residual block introduced by ResNet, shown in Figure 3B, adds a shortcut connection before the activation function of the next layer, transforming the input of the next layer from the original output H(X) = F(X) to H(X) = F(X) + X. By incorporating residual blocks and adding the original input X to the output, the network can better preserve and utilize the useful information from the original input, leading to more effective feature representations and improved performance and generalization ability. Furthermore, the subsequent input levels also include the original input X, enabling the network to learn mappings that retain the input information without fully recalculating the output. This allows the network to be easier to train and optimize, facilitating the construction of deeper network architectures.

Taking into account the task requirements and model complexity, this paper adopts the ResNet18 architecture from the ResNet model family. The overall structure of the ResNet18 network is shown in Figure 4a. Stage 1 can be considered the preprocessing stage, consisting of a 7×7 convolutional layer for feature extraction from the input data, followed by a max pooling layer to reduce the dimensionality of the feature map. Each stage from Stage 2 to Stage 5 contains two residual blocks: CONV BLOCK and ID BLOCK.

Each residual block consists of two 3 × 3 convolutional layers, with residual connections that allow the model to skip layers during training, facilitating the learning of identity mappings. The structures of the CONV BLOCK and ID BLOCK are shown in Figure 4b,c. The end of the network features a global average pooling layer and a fully connected layer. The global average pooling layer downsamples the feature map output by the last convolutional layer, while the fully connected layer maps the output feature vectors to the final class labels. Nuclide recognition based on neural network models is treated as a multi-class classification task, with a Softmax activation function added after the fully connected layer to convert the output into a probability distribution.

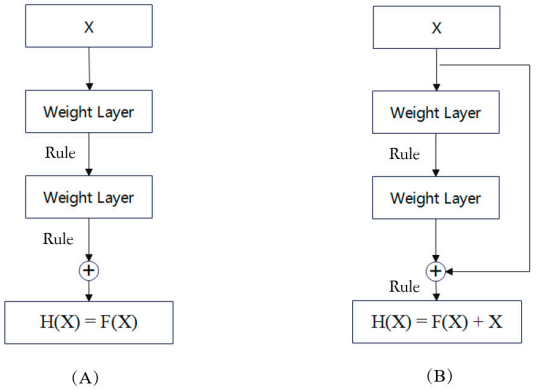


Figure 3. Structure diagram of traditional neural network and residual block: (**A**) traditional neural network; (**B**) residual neural network.

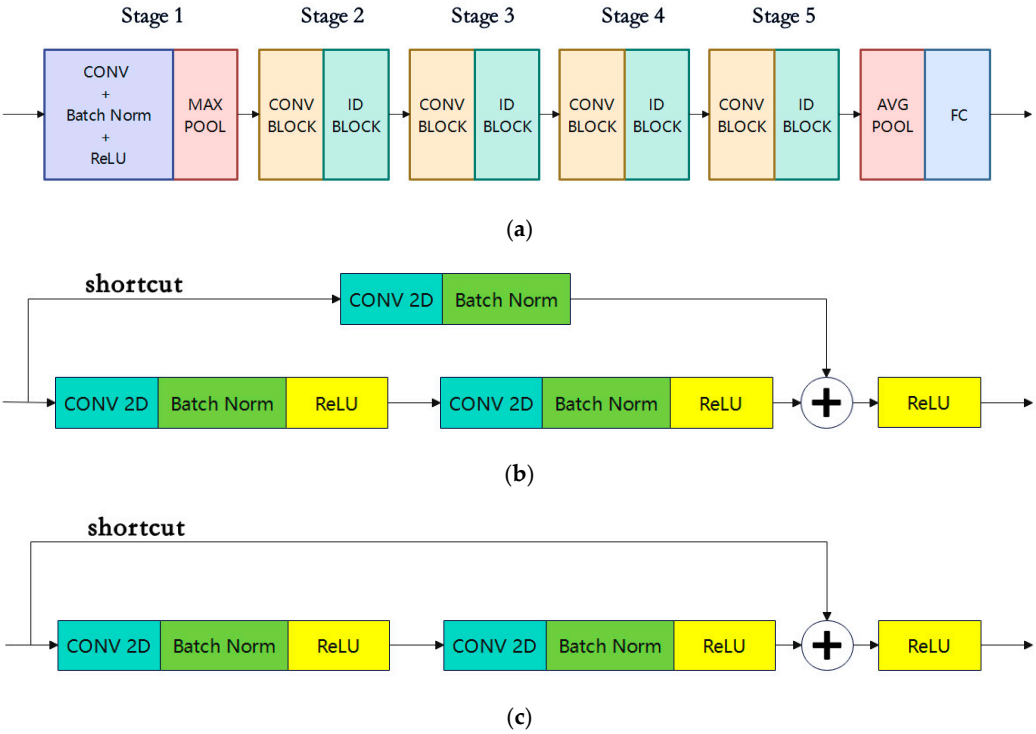


Figure 4. ResNet18 network model: (**a**) overall structure of the ResNet18 network; (**b**) CONV BLOCK structure; (**c**) ID BLOCK structure.

3.2. Evaluation

The neural network model features a complex structure and is widely applied. In practical applications, the quality of the network's training results becomes the primary focus.

Evaluation metrics provide a quantitative benchmark for model performance, effectively assessing its capabilities in specific tasks and helping to understand the model's accuracy, stability, and robustness. Nuclide recognition based on deep learning can be viewed as a multi-class classification task. In cases of imbalanced classes, a single accuracy measure often fails to reflect the true performance. Therefore, this paper introduces additional evaluation metrics, including precision, recall, F1 score, and loss, which are derived from neural network evaluation standards. These metrics offer a more comprehensive understanding of the model's performance across different classes, thereby enhancing the recognition capability of minority classes. The calculation methods and interpretations of each metric are presented in Table 1.

Table 1. Model evaluation metrics.

Metric	Calculation Method	Significance
Accuracy	$A = (TP + TN)/(TP + FP + TN + FN)$	The proportion of correct predictions among all predictions
Precision	$P = TP/(TP + FP)$	The proportion of predicted positive samples that are actually positive
Recall	$R = TP/(TP + FN)$	The proportion of actual positive samples that are correctly predicted
F1 Score	$F1 = 2 \times R \times P/(R + P)$	The harmonic mean of precision and recall

Loss quantifies the discrepancy between the model's predicted outcomes and the true labels, typically represented by a numerical value. A smaller loss indicates a more accurate prediction by the model. In deep learning-based nuclide recognition tasks, the loss is used to measure the difference between the predicted probabilities of each nuclide category and the actual category labels. In this context, TP refers to the number of correctly identified target nuclides, FP denotes the number of non-target nuclides incorrectly identified as target nuclides, TN indicates the number of correctly identified non-target nuclides, and FN represents the number of target nuclides that could not be identified.

4. Experimental Results and Analysis

4.1. Data Sources

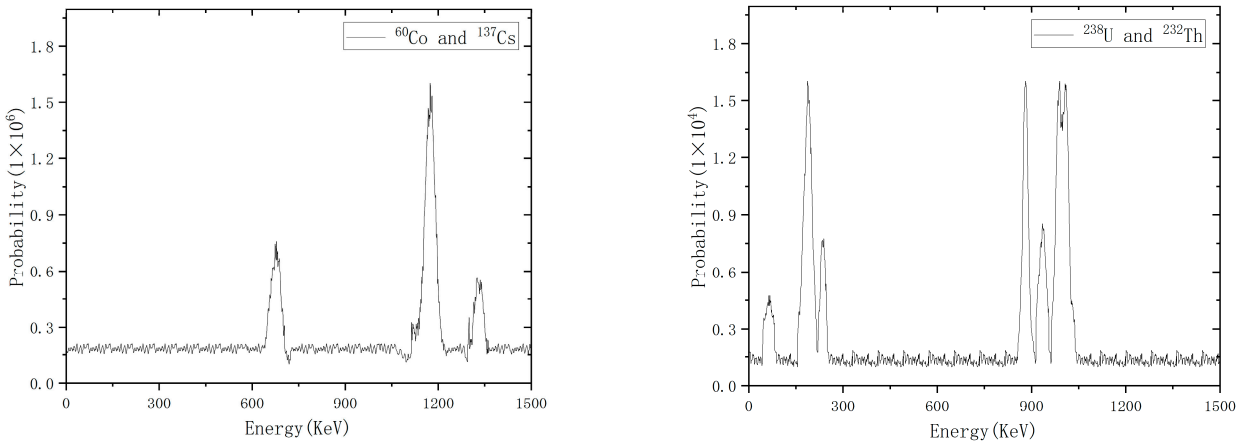
In nuclide identification research, obtaining experimental data presents numerous challenges. Firstly, the acquisition and management of radioactive sources involve high costs and strict safety regulations. Additionally, issues such as background noise, detector accuracy limitations, and sample imbalance affect data quality and model training. Furthermore, due to the wide variety of radioactive nuclides, it is not feasible to cover all possible nuclide combinations in a single experiment. In contrast, MCNP can generate gamma spectrum data for various nuclides under different experimental conditions. The reproducibility and controllability of MCNP allow for the collection of a large volume of training data without the constraints of laboratory settings. For example, Gao et al. (2018) [18] used MCNP to simulate gamma spectrum data for different nuclides and successfully applied it in the training of deep learning models. In this way, MCNP provides reliable experimental data support for nuclide identification research, offering high feasibility and advantages. Therefore, this paper chooses to use MCNP to obtain gamma spectrum data.

When using MCNP, background noise and detector efficiency, among other practical factors, are not considered. For high-resolution detectors, such as HPGe, the gamma spectra are clearer due to their higher energy resolution, making the spectral features more distinct. As a result, the task becomes relatively easier, which reduces the application value of neural networks. To introduce more challenges and enhance the effectiveness of neural networks in processing complex data, we choose to simulate the gamma spectra reactions of five single-source radionuclides using a NaI detector. These radionuclides include ^{137}Cs and ^{60}Co, which are widely used in nuclear power plants and radiation therapy; the

naturally-occurring radioactive isotopes ^{238}U and ^{232}Th; ^{226}Ra, which was once widely used in radiation therapy but has gradually been replaced by other radionuclides.

Considering that the two main peaks of ^{60}Co are relatively close and that the decay chains of ^{238}U, ^{232}Th, and ^{226}Ra produce multiple gamma rays that may overlap with those of other radionuclides, we use these five single-source radionuclides to form two-way and three-way combinations to introduce more interference between the nuclides, thus simulating a more realistic radiation environment. This results in a dataset of mixed gamma spectra from two and three sources, totaling 25,870 spectra, with each spectrum consisting of 1024 channels.

During the data simulation process, a NaI crystal with a cylindrical shape (diameter 6.52 cm, height 4 cm) was used as the detector. Different particle numbers (1×10^4 to 1×10^7) were set in the simulation, and various distances (1 cm to 18 cm) between the point source and the crystal were applied. To reflect the characteristic differences between the nuclides, different activity levels were assigned to the radionuclides: ^{60}Co, ^{137}Cs, and ^{226}Ra were set to an activity of 1×10^6 Bq, while ^{238}U and ^{232}Th had an activity of 5×10^6 Bq. It is worth noting that, for the ^{238}U nuclide, characteristic X-rays may arise from inner electron transitions, which could overlap with the gamma-ray peaks. However, due to the resolution limitations of the NaI detector, the influence of these characteristic X-rays on the spectrum is relatively small and does not significantly affect the primary gamma-ray features and the overall spectral shape. Nevertheless, to improve the precision of the gamma spectra, we performed background subtraction and peak fitting. Figure 5 shows the mixed spectra from two different nuclides at a distance of 5 cm. From the figure, it is evident that the simulated spectra's nuclide characteristic peaks are in good agreement with the actual situation.



(**a**) (**b**)

Figure 5. Example of a mixed gamma spectrum at a distance of 5 cm: (**a**) mixed gamma spectrum of ^{60}Co and ^{137}Cs; (**b**) mixed gamma spectrum of ^{238}U and ^{232}Th.

4.2. Original Model

The experimental data were divided into 70% for training and 30% for testing. Considering the convenience and resource requirements of the computational environment, the experiment was conducted using the following hardware configuration: CPU: 12th Gen Intel(R) Core(TM) i5-12500H, GPU: NVIDIA GeForce RTX 3050 Laptop. The Python version used was 3.9.18, and the ResNet18 model was built based on this version. The deep learning frameworks and related Python libraries involved include PyTorch version 1.12.0 + cu116, Torchvision version 0.13.0 + cu116, NumPy version 1.26.4, Pandas version 2.2.1, and other components. After the data underwent the aforementioned segmented GASF method for two-dimensional transformation, they were input into the ResNet18 model for training and

testing. The model's performance was evaluated and analyzed using precision, recall, F1 score, and loss metrics.

Through experimental testing, it was found that the learning rate (LR) did not converge when it exceeded 0.05. Therefore, the initial learning rate was set to 0.05. The Adam optimizer was used during training, with a dynamic decay strategy that reduces the learning rate to 30% of its previous value every 10 epochs to improve training efficiency. The loss function used was CrossEntropyLoss. To prevent overfitting, Dropout was applied, randomly dropping neurons to force the model to generalize better, with a dropout rate set to 0.5.

After 100 epochs, the results are shown in Figure 6. The model converged around the 55th epoch, achieving a precision of 99.9%, recall of 99.6%, F1 score of 99.7%, and a loss value of 0.0023 on the test set. These metrics reflect the model's efficient classification ability in the nuclide recognition task, demonstrating the powerful potential of deep learning techniques in complex feature extraction and pattern recognition. The overall recognition accuracy of the model reached 99.8%, validating the fact that the deep learning-based nuclide recognition model, combining residual networks and GASF technology, can achieve efficient and precise nuclide identification. The model's efficiency and reliability meet the standard recognition requirements.

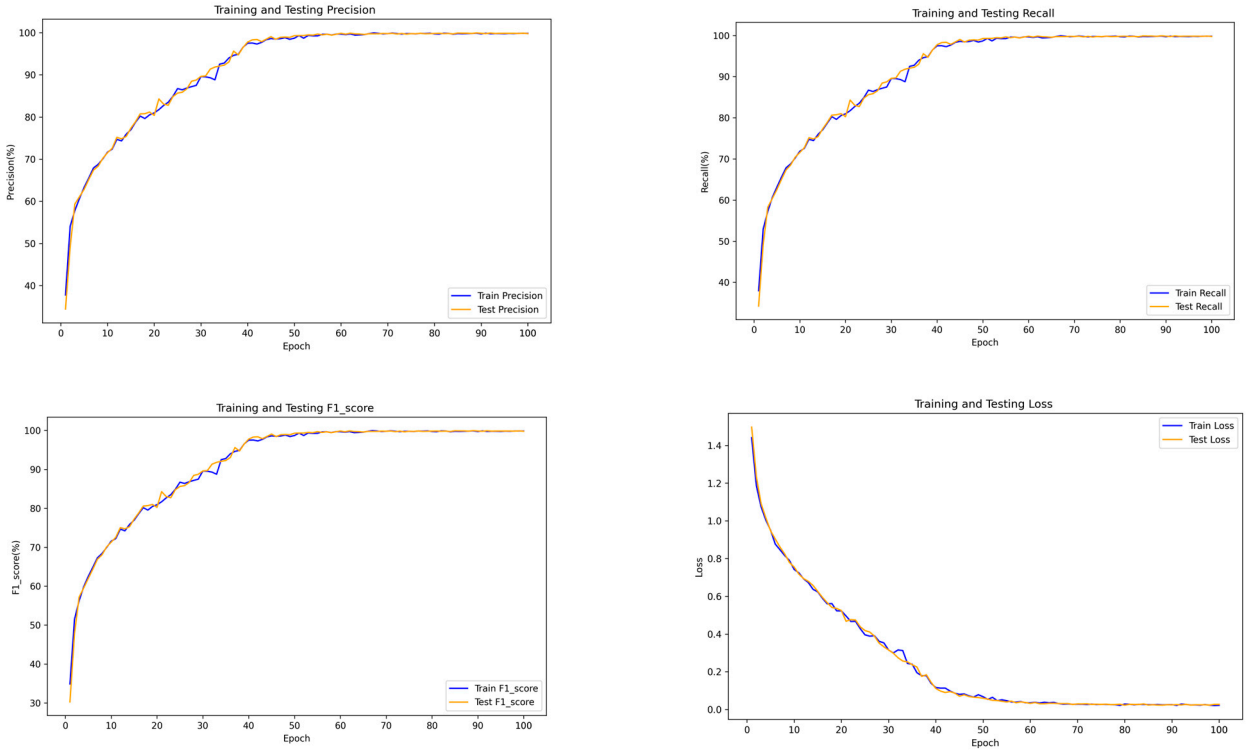


Figure 6. Evaluation metrics for nuclide identification results of the original model.

4.3. Improvethe Model

There is a relationship between the complexity of neural network models and their operating speed. According to the study by Han et al. (2016), reducing the number of parameters in the network can reduce the computational load, thereby improving speed while maintaining accuracy [19]. Furthermore, smaller convolutional kernels (e.g., 3×3) can more precisely capture local features, avoiding the potential information loss that may occur with larger kernels [20]. Removing pooling layers helps preserve more detailed information, thus enhancing the model's training performance [21]. In addition, reducing the number of channels in convolutional layers can lower model complexity and reduce the risk of overfitting [22]. In practical applications, such as medical imaging, single-photon emission computed tomography (SPECT) uses radioac-

tive isotope-labeled drugs to scan lesion areas [23], while positron emission tomography (PET) is used to observe metabolic changes in conditions like heart disease or tumors [24]; in these applications, high accuracy is required, but speed is also crucial. Therefore, optimizing the model structure and improving inference speed is essential.

Based on the application requirements, the model was improved. In the ResNet18 model, the number of channels in the convolutional layers from stage 1 to stage 5 was originally 64, 64, 128, 256, and 512, respectively. These were modified to 16, 16, 32, 64, and 128, respectively. Additionally, considering the size of the dataset used in this paper, the 7×7 convolution and max pooling operations in stage 1 of the ResNet18 network were prone to losing some feature information. Therefore, in the improved model, the 7×7 convolution was replaced with a 3×3 convolution, with a stride and padding of 1, and the max pooling layer was removed. This modification helps to preserve as much of the original image feature information as possible. A comparison of the network model structure parameters before and after the improvement is shown in Table 2.

Table 2. Comparison of network models before and after improvement.

Layer Name	Original Model	Improved Model
Conv1	$7 \times 7, 64, \mathrm{s} = 2, \mathrm{p} = 3$ $3 \times 3, \text{Max pooling}, \mathrm{s} = 2, \mathrm{p} = 1$	$3 \times 3, 16, \mathrm{s} = 1, \mathrm{p} = 1$
Conv2	$\begin{bmatrix} 3 \times 3, & 64 \\ 3 \times 3, & 64 \end{bmatrix} \times 2$	$\begin{bmatrix} 3 \times 3, & 16 \\ 3 \times 3, & 16 \end{bmatrix} \times 2$
Conv3	$\begin{bmatrix} 3 \times 3, & 128 \\ 3 \times 3, & 128 \end{bmatrix} \times 2$	$\begin{bmatrix} 3 \times 3, & 32 \\ 3 \times 3, & 32 \end{bmatrix} \times 2$
Conv4	$\begin{bmatrix} 3 \times 3, & 256 \\ 3 \times 3, & 256 \end{bmatrix} \times 2$	$\begin{bmatrix} 3 \times 3, & 64 \\ 3 \times 3, & 64 \end{bmatrix} \times 2$
Conv5	$\begin{bmatrix} 3 \times 3, & 512 \\ 3 \times 3, & 512 \end{bmatrix} \times 2$	$\begin{bmatrix} 3 \times 3, & 128 \\ 3 \times 3, & 128 \end{bmatrix} \times 2$
Average Pooling, Fc, Softmax		

Using the same dataset, data split ratio, and preprocessing methods, the improved model was trained and tested. The experimental results are shown in Figure 7, where the precision is 99.3%, recall is 99.7%, the F1 score is 99.5%, and the loss value is 0.0031.

In the improved model, the recognition results of single-source and double-source nuclides on the test set are presented through confusion matrix plots, as shown in Figure 8. According to the results, the feature peaks of single-source nuclides are relatively clear, and all samples are correctly classified, achieving 100% recognition accuracy. In the case of double-source combinations, when the feature peaks of the nuclides included in the combination are relatively close, the gamma spectra of the two different nuclides may overlap in certain energy ranges, thereby increasing the difficulty of classification for the model. The analysis of the confusion matrix reveals that misclassified samples are usually concentrated among nuclide combinations with similar feature peaks. For example, in the case of ^{60}Co + ^{137}Cs and ^{60}Co + ^{226}Ra, although the two main gamma peaks of ^{60}Co are relatively distinct, the main peak of ^{137}Cs and some low-energy lines of ^{226}Ra may overlap. A similar situation also occurs in other combinations with close nuclide features, such as ^{137}Cs + ^{232}Th and ^{226}Ra + ^{238}U. Despite the existence of misclassifications, their proportion is minimal. Through the analysis of the confusion matrix, it is confirmed that nuclide combinations with similar feature peaks are more likely to lead to misclassification, which provides valuable insights for further optimizing the model in the future.

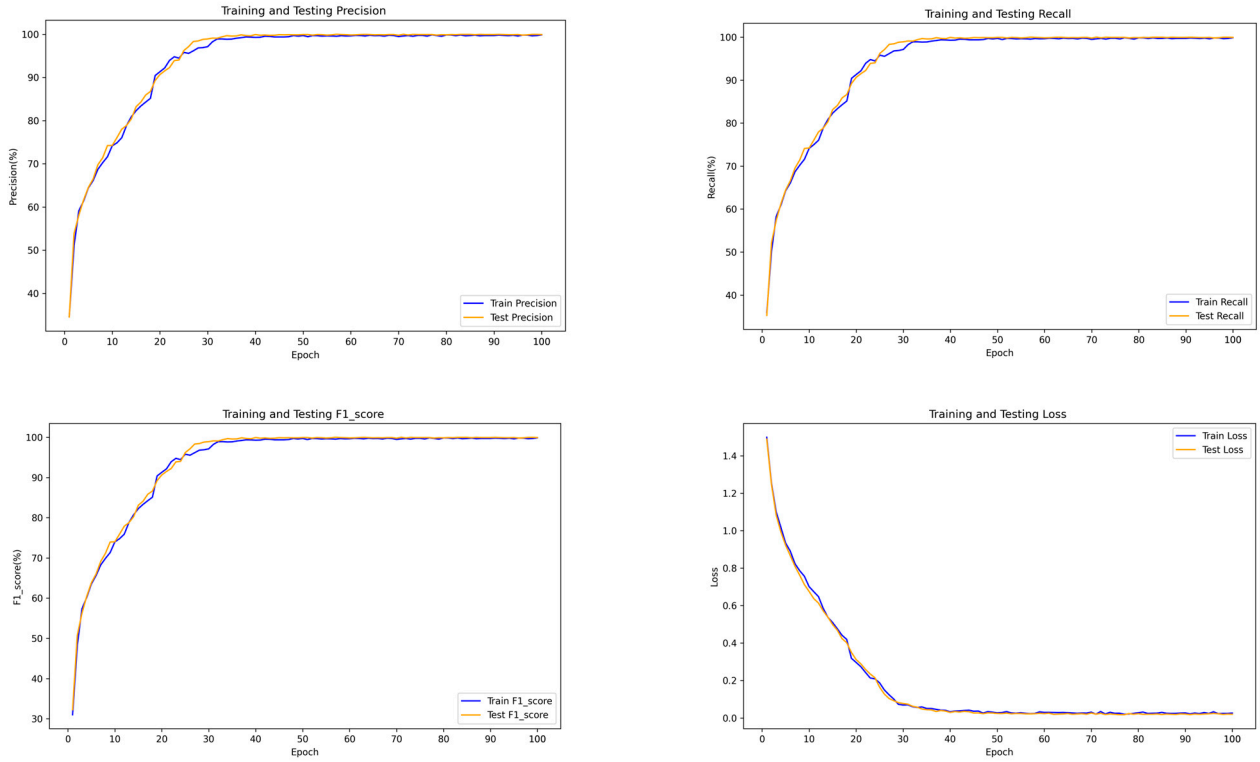
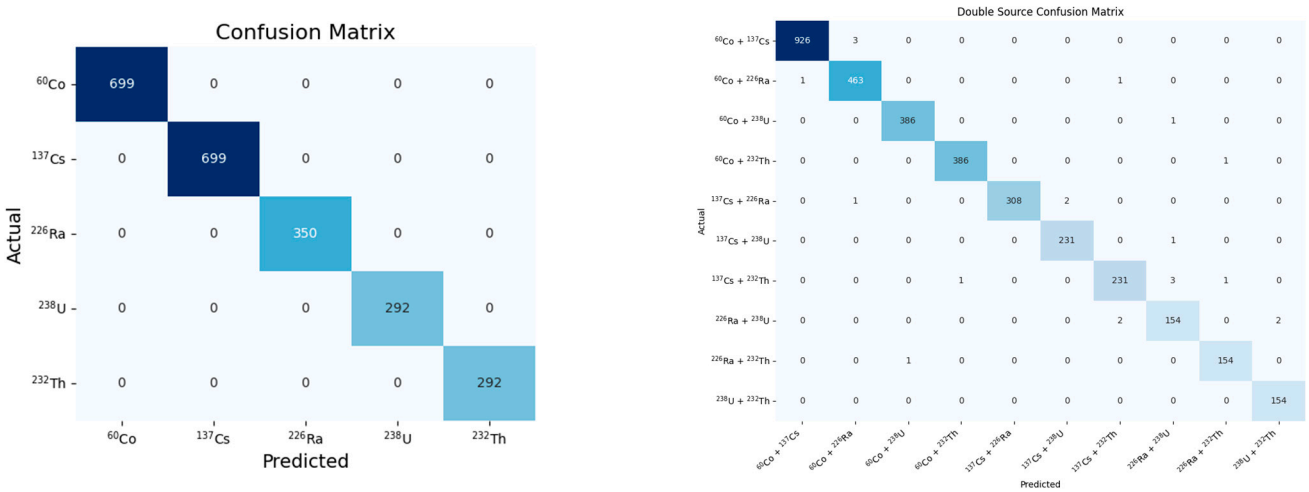


Figure 7. Evaluation metrics for the nuclide identification results of the improved model.



(**a**) (**b**)

Figure 8. Recognition results of the improved model on the test set: (**a**) single-source recognition results; (**b**) double-source recognition results.

A comparison of the model's performance before and after improvement is presented in Table 3. Compared to the original model, the improved model reduced the number of parameters by over 90%, and its size was reduced by nearly 40 MB. After running for the same number of epochs, the improved model converged in approximately 40 epochs, with the overall training time reduced by 292 s, demonstrating a faster convergence rate. Furthermore, the overall recognition accuracy still reached 99.5%, with no significant decline.

Table 3. Comparison of model results and parameters before and after improvement.

	Precision/%	Recall/%	Accuracy/%	Number of Parameters/10^5	Model Size/MB	Time for 100 Epochs/S
Original Model	99.9	99.6	99.8	111.81	42.65	10,633
Improved Model	99.3	99.7	99.5	7.15	2.73	10,341

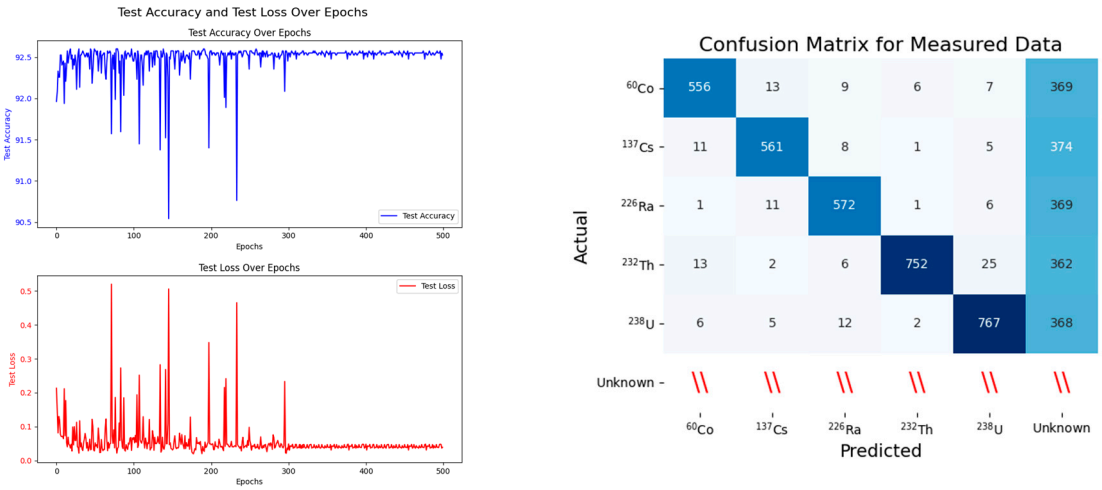
4.4. Verification with Experimental Data

To evaluate the practical application performance of the proposed nuclide identification model, this study further introduces spectral data obtained from actual measurements for validation. The measured data were provided by a laboratory. Specifically, gamma spectrum data for ^{60}Co, ^{137}Cs, and ^{226}Ra were collected by the laboratory using a gamma spectroscopy acquisition system for each radioactive source, with 600 spectra for each point source. The gamma spectrum data for ^{238}U and ^{232}Th were obtained from a sandstone uranium ore logging model established by a radiation exploration metrology station, with 800 spectra for each point source. In total, 3400 spectra were collected for the five radioactive sources. To conduct a more comprehensive validation, three additional radionuclides that were not present in the training set were introduced: ^{152}Eu, ^{133}Ba, and ^{241}Am. These data were also provided by the laboratory, with 600 spectra for each radioactive source, resulting in a total of 1800 spectra for the three new categories. The inclusion of these new categories helps to test the model's generalization ability and assess its performance when faced with new nuclides not seen during training.

The 1800 spectra of the three new categories were evenly distributed among the existing categories of ^{60}Co, ^{137}Cs, ^{226}Ra, ^{238}U, and ^{232}Th. Since the training set consists of only five categories, the newly introduced nuclides could only be misclassified as one of the existing categories. To test whether the model can correctly identify the new nuclides without misclassifying them as existing categories, this study follows a common approach in machine learning and deep learning: when the number of categories in the test set exceeds that of the training set, the three new radionuclides are defined as an "unknown" category. Specifically, for each input gamma spectrum sample, the model outputs the predicted probability for each category. To ensure that new nuclides are not misclassified as known categories, a minimum probability threshold is set. When the maximum predicted probability for a sample is below this threshold, the sample is considered to belong to the "unknown" category, and the prediction result is labeled as "unknown nuclide" instead of being classified as one of the existing categories [25–30].

Prior to the official testing, a preliminary test was conducted on 3400 gamma spectra data from five radionuclides: ^{60}Co, ^{137}Cs, ^{226}Ra, ^{232}Th, and ^{238}U. The preliminary test was performed three times, each running for 300 epochs, and the overall accuracy of the model in all three rounds of testing was approximately 95.2%, with the loss value approaching 0.05. During this process, the predicted probability corresponding to each correctly classified sample was recorded. The results showed that, for 95% of the correctly classified samples, the predicted probability output by the model was higher than 0.6. Based on this statistical result, the minimum probability threshold was set to 0.6 to ensure that the new nuclides would not be misclassified as existing categories.

The mixed data of the ^{60}Co, ^{137}Cs, ^{226}Ra, ^{238}U, and ^{232}Th gamma spectra with the three newly introduced radionuclides, ^{152}Eu, ^{133}Ba, and ^{241}Am, were processed using the aforementioned segmented GASF method and input into the trained improved model for testing. After 500 epochs, the test results are shown in Figure 9. Figure 9a displays the accuracy and loss metrics curves, while Figure 9b presents the confusion matrix with the recognition results of the actual measurement data along with the recorded "unknown" category.



(**a**) (**b**)

Figure 9. Testing results with experimental data: (**a**) accuracy and loss curves; (**b**) confusion matrix of test results.

The results show that the model exhibits significant fluctuations in accuracy and loss during the first 300 epochs, which may be attributed to noise in the measured data, environmental interference, and the impact of newly introduced radionuclides. However, after training for 300 epochs, the model gradually converges, reaching an accuracy of 92.6% at 500 epochs, with the loss stabilizing around 0.05, indicating good convergence and demonstrating the model's strong predictive capability. Further analysis of the confusion matrix reveals that the model performs well overall. For known radionuclides, the model shows high stability and accuracy in recognition, with the number of correct identifications for all known radionuclides closely matching the actual samples in the test data. For the mixed data, the model is able to correctly classify it as the "unknown" category. Of the 5200 test samples, 1800 contain newly introduced data from three categories. Statistical analysis shows that 1842 samples were marked as the "unknown" category, resulting in a recognition error rate of 2.33% for the new radionuclides.

Overall, although the accuracy of the measured data is slightly lower than that of the simulated data, this difference can be attributed to the complex noise and environmental interference present in the measured data, such as instrument errors and inconsistencies in the radiation source characteristics. Nevertheless, the model still demonstrates a high accuracy of 92.6% and is able to identify unknown radionuclides, proving its robustness and generalization capability in practical applications. In the future, further improvement in the model's accuracy for unseen categories can be achieved by incorporating more radionuclide samples into the training process.

5. Discussion

This paper proposes a deep learning-based nuclide identification method that combines Residual Networks (ResNets) and Gramian Angular Summation Field (GASF) techniques. After dimensionality reduction of the gamma spectrum using the Piecewise Aggregate Approximation (PAA) algorithm, GASF is employed to transform the spectrum into two-dimensional images. This approach fully exploits the spatial features and dependencies within the data, exploring a new pathway for data processing in the field of nuclide identification. The experimental results show that the model achieves a recognition accuracy of 99.5% on the simulated data. When tested with actual measurement data containing unknown radionuclides, it still maintains an accuracy of 92.6% and is capable of

successfully identifying the unknown radionuclides. This result validates the advantages and effectiveness of the proposed method in handling complex, noisy, real-world data.

Additionally, the model proposed in this paper relies on large-scale labeled datasets for training, but, in practical applications, collecting and labeling high-quality, real-world gamma spectrum data may present challenges. Future research directions could explore how to use a small amount of labeled data for effective transfer learning or self-supervised learning, thereby improving the model's performance in data-scarce environments.

Author Contributions: All authors contributed to the manuscript and discussed the results. Conceptualization, S.Z. (Shuqiang Zhao); methodology, S.Z. (Shuqiang Zhao); validation, S.Z. (Shuqiang Zhao); R.C. provided criticism and revised the manuscript; funding acquisition, S.Z. (Shumin Zhou). All authors have read and agreed to the published version of the manuscript.

Funding: This research was funded by the National Natural Science Foundation of China, grant number 12165001.

Institutional Review Board Statement: The study did not require ethical approval.

Informed Consent Statement: The study did not involve humans.

Data Availability Statement: The original contributions presented in this study are included in the article. Further inquiries can be directed to the corresponding authors.

Conflicts of Interest: The authors declare no conflict of interest.

References

1. Iyer, J.K.S.N.; Suri, S.; Gupta, P. Nuclear security and safeguards in the age of the nuclear renaissance. *Sci. Glob. Secur.* **2017**, *25*, 113–130.
2. Nilsson, J.S.; Nilsson, L.; Jonsson, A. Environmental monitoring of nuclear waste and radiation accidents. *Sci. Total Environ.* **2017**, *601–602*, 258–267.
3. Nunes, P.J.H.; Costa, L.M.; Lima, J.A. Use of radiopharmaceuticals in diagnostic imaging. *Eur. J. Nucl. Med. Mol. Imaging* **2016**, *43*, 26–38.
4. Sargent, R.A.S.; Smith, M. Radiation detection in industrial applications. *J. Radiol. Prot.* **2012**, *32*, 337–350.
5. Yue, C.; Niu, D. A review of radioactive nuclide gamma spectrum analysis methods. *Ordnance Autom.* **2023**, *42*, 44–47.
6. Liu, Y.; Wang, W.; Niu, D. Nuclide recognition analysis method based on artificial neural networks. *Ordnance Autom.* **2015**, *34*, 86–91.
7. Wang, Y.; Wei, Y. Nuclide recognition based on fuzzy logic in γ-ray energy spectra. *J. Tsinghua Univ.* **2012**, *52*, 1736–1740.
8. Zhou, W.; Zhou, D.; Kang, J. Research on a nuclide recognition algorithm based on logistic regression binary classification. *Nucl. Electron. Detect. Technol.* **2023**, *43*, 12–17.
9. Zhou, S. Research on Nuclide Recognition Method Based on Multi-Class Weight Label Fuzzy Decision Tree. Master's Thesis, Southwest University of Science and Technology, Mianyang, China, 2022.
10. Ren, J.; Zhang, J.; Wang, K. Nuclide recognition algorithm based on SVD and SVM. *Ordnance Autom.* **2017**, *36*, 50–53.
11. Wen, S.; Wang, B.; Xiao, G.; Shen, C. Research on nuclide recognition algorithm based on sequential Bayesian methods. *Nucl. Electron. Detect. Technol.* **2016**, *36*, 179–183.
12. Wang, Y.; Ouyang, C.; Liu, Z.; Wan, Y. Energy spectrum nuclide recognition method based on long short-term memory neural network. *High Power Laser Part. Beams* **2020**, *32*, 154–161.
13. Du, X.; Liang, M.; Li, K.; Yu, Y.; Liu, X.; Wang, X.; Wang, R.; Zhang, G.; Fu, Q. γ-ray radioactive nuclide recognition method based on convolutional neural networks. *J. Tsinghua Univ.* **2023**, *63*, 980–986.
14. Hu, H.X.; Zhang, J.M.; Wang, K.P.; Feng, X.H. Application of convolutional neural networks in complex nuclide recognition. *Sens. Microsyst.* **2019**, *38*, 154–156+160.
15. Wang, Z.G.; Yan, W.Z.; Oates, T. Time series classification from scratch with deep neural networks: A strong baseline. In Proceedings of the 2017 International Joint Conference on Neural Networks (IJCNN), Anchorage, AK, USA, 14–19 May 2017; IEEE Press: New York, NY, USA, 2017; pp. 1578–1585.
16. You, H.; Fan, G. Gamma spectrum analysis of copper ore based on neural networks. *Electron. Technol. Softw. Eng.* **2023**, *2*, 125–129.
17. He, K.M.; Zhang, X.Y.; Ren, S.Q.; Sun, J. Deep residual learning for image recognition. In Proceedings of the 2016 IEEE Conference on Computer Vision and Pattern Recognition (CVPR), Las Vegas, NV, USA, 27–30 June 2016; IEEE: Piscataway, NJ, USA, 2016.
18. Gao, Y.; Li, X.; Zhang, Z.; Wang, J. Gamma spectrum simulation and identification of nuclear materials using MCNP and deep learning. *Nucl. Instrum. Methods Phys. Res. Sect. A* **2018**, *895*, 21–28.

19. Han, S.; Mao, H.; Dally, W.J. Deep Compression: Compressing Deep Neural Networks with Pruning, Trained Quantization and Huffman Coding. *arXiv* **2016**, arXiv:1510.00149.
20. Szegedy, C.; Liu, W.; Jia, Y.; Sermanet, P.; Reed, S.; Anguelov, D.; Erhan, D.; Vanhoucke, V.; Rabinovich, A. Going deeper with convolutions. In Proceedings of the IEEE Conference on Computer Vision and Pattern Recognition (CVPR) 2015, Boston, MA, USA, 7–12 June 2015; IEEE: Piscataway, NJ, USA, 2015; pp. 1–9.
21. Springenberg, J.T.; Dosovitskiy, A.; Riedmiller, M.; Fischer, P. Striving for Simplicity: The all Convolutional Net. *arXiv* **2014**, arXiv:1412.6806.
22. Howard, A.G.; Zhu, M.; Chen, B.; Kalenichenko, D.; Wang, W.; Weyand, T.; Andreetto, M.; Adam, H. MobileNets: Efficient Convolutional Neural Networks for Mobile Vision Applications. *arXiv* **2017**, arXiv:1704.04861.
23. Liu, Z.; Wang, S.; Li, L.; Zhang, Y. Application of SPECT in early detection of lung cancer. *J. Nucl. Med.* **2020**, *61*, 469–475.
24. Levin, C.S.; Wang, Y.; Adams, M.A.; Lee, K. PET/CT imaging in cardiovascular disease. *J. Cardiovasc. Imaging* **2019**, *27*, 84–92.
25. Zhou, Z.; Zhang, M. A k-nearest neighbor approach for uncertain data classification. *J. Mach. Learn. Res.* **2002**, *3*, 1351–1365.
26. Ren, Z.; Liu, S. Handling out-of-distribution and unseen data in deep neural networks. *IEEE Trans. Neural Netw. Learn. Syst.* **2017**, *28*, 1787–1798.
27. Hsu, C.W.; Lin, C.J. A comparison of methods for multiclass support vector machines. *IEEE Trans. Neural Netw.* **2010**, *13*, 421–434.
28. Lee, D.; Choi, J. Classifying unseen categories in deep learning: A threshold-based approach. *Neural Comput. Appl.* **2018**, *30*, 2675–2682.
29. Bengio, Y.; Courville, A. *Deep Learning*; MIT Press: Cambridge, MA, USA, 2016.
30. Liu, Z.; Yang, Y. Improving generalization in neural networks with uncertainty estimation. *Proc. IEEE Int. Conf. Comput. Vis.* **2018**, *34*, 511–519.

Disclaimer/Publisher's Note: The statements, opinions and data contained in all publications are solely those of the individual author(s) and contributor(s) and not of MDPI and/or the editor(s). MDPI and/or the editor(s) disclaim responsibility for any injury to people or property resulting from any ideas, methods, instructions or products referred to in the content.